

Deep-ultraviolet Raman spectra of Mars-relevant evaporite minerals under 248.6 nm excitation

Joseph Razzell Hollis^{a,*}, Schelin Ireland^{a,b}, William Abbey^a, Rohit Bhartia^c, Luther W. Beegle^a

^a NASA Jet Propulsion Laboratory, California Institute of Technology, Pasadena, CA, United States of America

^b University of Hawaii at Mānoa, Mānoa, HI, United States of America

^c Photon Systems Inc., Covina, CA, United States of America

ABSTRACT

We have measured the deep-ultraviolet (DUV) Raman spectra of a number of evaporite minerals that are relevant to lacustrine and fluvial environments found on Earth and Mars, and show that DUV Raman can provide detailed information on elemental composition and crystal structure. The minerals included three borates, eight carbonates, and seven sulfates, with each class of mineral exhibiting very distinct spectra under 248.6 nm excitation, dominated by the various internal vibrations of the borate, carbonate or sulfate oxyanion. Major peak positions were similar to values reported under visible excitation: 1079 cm^{-1} for calcite, 1006 cm^{-1} for gypsum and 1078 cm^{-1} for colemanite. Within each class, minerals consisting of different metallic cations could be distinguished by the position of the dominant vibrational mode and the relative intensities of the minor modes, ascribed to the electrostatic impact of the cation on the vibrational behavior of the oxyanion. There was also evidence that DUV Raman can reveal minor metallic components even if they are not apparent in XRD, as two of three calcite (CaCO_3) samples exhibited a shoulder on the dominant peak consistent with perturbation by Mg. UV absorption by $\text{Fe}^{2+/3+}$ was a major factor in determining measurable signal, with Fe-rich minerals exhibiting weak/undetectable spectra. Understanding the spectra of these evaporite minerals will be essential to interpreting and identifying complex mineral samples using this technique, and represents an important addition to the spectral standards library of DUV Raman spectroscopy.

1. Introduction

Deep-ultraviolet (DUV) Raman spectroscopy is a fairly recent development in vibrational spectroscopy, exploiting the enhancement in signal attained by using high-energy excitation to increase overall sensitivity to achieve reliable chemical detection and identification even at low laser power (Asher, 1984; Asher, 1993; Abbey et al., 2017; Razzell Hollis et al., 2020). The obvious application of this technique to astrobiology, particularly the search for the chemical biosignatures of past or extant life on other worlds, has led to a DUV Raman instrument named *SHERLOC* being selected as part of the scientific payload of NASA's upcoming *Mars 2020* mission (Beegle et al., 2015). However, the innate variation of Raman spectra with excitation wavelength means that pre-existing spectral standard libraries taken using visible excitation cannot be employed when identifying compounds from DUV Raman spectra, and a new library must be created. Efforts have so far focused on obtaining standard spectra of organic compounds, particularly aromatic organics that are relevant to biological processes, such as DNA nucleobases and amino acids (Asher, 1993; Wen and Thomas, 1998; Sapers et al., 2019), and little has been published on the DUV Raman spectra of minerals that may harbor and/or preserve ancient organic material

(Abbey et al., 2017). In this paper we will report in detail the DUV Raman spectra for a number of evaporite minerals that are intimately associated with aqueously modified environments on Earth, and may represent potential mineral matrices for the preservation of organic matter on Mars (Westall et al., 2015; Hays et al., 2017; Gasda et al., 2017).

Minerals chosen for this study include borates, carbonates, sulfates, halides (halite), and silicates (quartz). Borates, carbonates, sulfates and halides can form under aqueous conditions and are common in lacustrine evaporite deposits here on Earth. They are also likely to occur in similar environments on Mars, such as those that occur in association with the deltaic deposits in Jezero Crater, the planned *Mars 2020* landing site. The presence of borates on Mars has been suggested through analysis of Martian meteorites and, more recently, by in situ results from the Curiosity Rover in Gale Crater (Stephenson et al., 2013; Gasda et al., 2017). On Earth, boron is suspected to be an important element for the origin of life, so on Mars local enrichment may be indicative of an increase in habitability potential (Kim et al., 2016). Carbonates, such as calcite, have been identified at the *Phoenix* landing site, in Columbia Hills, and in the Isidis Basin, adjacent to Jezero Crater (Ehlmann et al., 2008; Boynton et al., 2009; Niles et al., 2013). Sulfate

DOI of original article: <https://doi.org/10.1016/j.icarus.2020.113969>.

* Corresponding author

E-mail address: hollis@jpl.nasa.gov (J. Razzell Hollis).

<https://doi.org/10.1016/j.icarus.2020.114067>

minerals, such as gypsum and anhydrite, have been identified throughout Gale Crater by the *Curiosity* Rover and are believed to be ubiquitous on Mars, representing evaporite deposits formed from ancient acidic lakes (Vaniman et al., 2013; Ehlmann and Edwards, 2014). Chloride bearing deposits, such as halite, have been identified throughout the Southern Hemisphere of Mars (Osterloo et al., 2010), and remain a likely end member for any proposed evaporite sequence. For comparison, we also examined quartz, a silicate mineral not typically associated with evaporite deposits but is a product of hydrothermal alteration.

2. Materials and methods

The minerals used in this study are given in Table 1, along with their chemical compositions and origins. Compositions were confirmed by XRD measurements.

The three borates examined were colemanite ($\text{CaB}_3\text{O}_4(\text{OH})_3 \cdot \text{H}_2\text{O}$), kernite ($\text{NaCaB}_5\text{O}_6(\text{OH})_6 \cdot 5\text{H}_2\text{O}$), and ulexite ($\text{Na}_2\text{B}_4\text{O}_6(\text{OH})_2 \cdot 3\text{H}_2\text{O}$). The seven carbonates minerals examined were calcite (CaCO_3), dolomite ($\text{CaMg}(\text{CO}_3)_2$), magnesite (MgCO_3), nahcolite (NaHCO_3), rhodochrosite (MnCO_3), siderite (FeCO_3), and trona ($\text{Na}_2\text{CO}_3 \cdot \text{NaHCO}_3 \cdot 2\text{H}_2\text{O}$). The six sulfates were anhydrite (CaSO_4), barite (BaSO_4), epsomite ($\text{MgSO}_4 \cdot 7\text{H}_2\text{O}$), gypsum ($\text{CaSO}_4 \cdot 2\text{H}_2\text{O}$), jarosite ($\text{KFe}_3(\text{OH})_6(\text{SO}_4)_2$), and thenardite (Na_2SO_4). Minerals were measured as single crystals and as powders, where available, and for calcite and dolomite we also measured sedimentary samples (referred to as “calcite chalk” & “dolomite rock” respectively).

2.1. X-ray diffraction

The identity of the minerals used in this study were confirmed by X-ray diffraction measurements. Powder X-ray diffraction patterns were obtained using a Bruker AXS model D8 Discover X-ray diffractometer equipped with a graphite monochromator and a General Area Detector Diffraction System. Radiation applied was $\text{CuK}\alpha$ ($\lambda = 1.5404 \text{ \AA}$) operated at 40 kV and 20 mA. Phase identification was accomplished by comparing the $13\text{--}75^\circ$ 2θ range with standard powder diffraction files from the International Centre for Diffraction Data (2000) using the DIFFRAC^{plus} EVA 13 Evaluation Package from Bruker AXS (2007).

2.2. DUV measurements

MOBIUS, a custom DUV resonant Raman spectrometer at the NASA Jet Propulsion Laboratory was used for all measurements. MOBIUS uses a 248.579 nm NeCu pulsed laser (Photon Systems Inc.) reflected off of a 248.58 nm RazorEdge ultra-steep long-pass edge filter (Semrock Inc.) and focused onto the sample through a DUV chromatically corrected $f/4$ objective lens with a numerical aperture of 0.13 (ThorLabs LMU-5 \times -UVB). The laser spot is annular, taking the form of a Gaussian-blurred ellipse with semi-major and semi-minor diameters of 44 and 32 μm respectively, and a radial standard deviation of 7.4 μm (Razzell Hollis et al., 2020). Raman-scattered photons were collected in a 180° back-scatter geometry, passed through a Horiba 550i spectrometer and recorded by a Horiba Symphony e2v 42–10 CCD liquid nitrogen cooled (-140°C) detector. The collected light was passed through a slit with a width of 250 μm , and diffracted by a grating with a groove density of 1800 lines/mm. Raman spectra were obtained over 1024 points between $\sim 610 \text{ cm}^{-1}$ (252.4 nm) and $\sim 4220 \text{ cm}^{-1}$ (277.7 nm) with a spectral bin size of 3.8 cm^{-1} . Prior to data collection, an initial calibration was done by validating the position of the primary and secondary laser lines at 248.58 and 252.93 nm respectively. Raman spectra were integrated over 1200 pulses per point with a frequency of 40 Hz, a pulse width of 40 μs , and an incident pulse energy of 1.9–2.8 μJ . We note that the grain size of the powdered samples was of a similar order of magnitude to the size of the laser spot in our DUV Raman spectrometer, $\sim 40 \mu\text{m}$, and so for all samples we obtained 100 spectra in a 10×10 grid over an area of 1×1

Table 1

Mineral samples used in this study, their origins and any minor/trace components as detected by XRD. * indicates synthetic samples.

	Name	Chemical formula	Origin
Borates	Colemanite	$\text{Ca}[\text{B}_3\text{O}_4(\text{OH})_3] \cdot \text{H}_2\text{O}$	Corkscrew Mine, Death Valley, California (JPL Collection). Also contains minor inyoite ($\text{Ca}[\text{B}_3\text{O}_3(\text{OH})_5] \cdot 4\text{H}_2\text{O}$)
	Kernite	$\text{NaCa}[\text{B}_5\text{O}_6(\text{OH})_6] \cdot 5\text{H}_2\text{O}$	Borax Mine, Boron, California (JPL Collection). Also contains minor tinalconite ($\text{Na}_2[\text{B}_4\text{O}_5(\text{OH})_4] \cdot 3\text{H}_2\text{O}$)
	Ulexite	$\text{Na}_2[\text{B}_4\text{O}_6(\text{OH})_2] \cdot 3\text{H}_2\text{O}$	Death Valley region, California (JPL Collection)
Carbonates	Calcite	CaCO_3	Santa Eulalia, Chihuahua, Mexico (WARDS #49–5860)
	Calcite (chalk)	CaCO_3	Dover, England (WARDS #46–1449)
	Dolomite	$\text{CaMg}(\text{CO}_3)_2$	Butte, Montana (WARDS #49–5871)
	Magnesite	MgCO_3	Brumado, Bahia, Brazil (WARDS #49–5923)
	Nahcolite*	NaHCO_3	Arm & Hammer Baking Soda
	Rhodochrosite	MnCO_3	Sweet Home Mine, Alma, Colorado (WARDS)
	Siderite	FeCO_3	Ivigtut, Greenland (WARDS #49–5911). Also contains trace amounts of hematite (Fe_2O_3)
	Trona*	$\text{Na}_2\text{CO}_3 \cdot \text{NaHCO}_3 \cdot 2\text{H}_2\text{O}$	JPL Collection. Also contains minor thernonatrite ($\text{Na}_2\text{CO}_3 \cdot \text{H}_2\text{O}$)
Sulfates	Anhydrite	CaSO_4	Balmat, New York (WARDS #46–0538). Also contains minor (<15%) gypsum ($\text{CaSO}_4 \cdot 2\text{H}_2\text{O}$)
	Barite*	BaSO_4	Wako Pure Chemicals #022–00425
	Epsomite*	$\text{MgSO}_4 \cdot 7\text{H}_2\text{O}$	CVS Epsom Salts
	Gypsum	$\text{CaSO}_4 \cdot 2\text{H}_2\text{O}$	Tawas City, Michigan (WARDS #46–3798)
	Melanterite	$\text{FeSO}_4 \cdot \text{H}_2\text{O}$	JPL Collection. Also contains minor rozenite ($\text{FeSO}_4 \cdot 4\text{H}_2\text{O}$) and trace szomolnokite ($\text{FeSO}_4 \cdot \text{H}_2\text{O}$)
	Natrojarosite	$(\text{Na},\text{K})\text{Fe}_3(\text{OH})_6(\text{SO}_4)_2$	Tibet (Caltech Collection)
Halide	Thenardite	Na_2SO_4	JPL Collection
	Halite	NaCl	Window, Ontario, Canada (WARDS #46–3823)
Silicate	Quartz	SiO_2	Minas Gerais, Brazil (WARDS #49–5886)

mm, to ensure a representative average was obtained.

2.3. Data processing

For each individual spectrum, spectral intensities were normalized according to the total output energy of the laser during the measurement, recorded pulse by pulse using a photo-diode at the exit aperture of

the laser and calibrated to the intensity at the sample as measured prior by an Ophir sensor. Cosmic rays were identified as outliers in the distribution of intensity values in each Raman shift channel (Uckert et al., 2019) and replaced by the average value of adjacent points. Further processing was done by in-house Python scripts utilizing Numpy (van der Walt et al., 2011), SciPy (Jones et al., 2001), and LMFIT (Newville et al., 2014) packages. First, a linear correction was applied to Raman shift values to account for optical distortion across the detector, based on the standard positions of the 919, 1374, 2252, and 2942 cm^{-1} bands of acetonitrile. Outlier spectra in each scan, e.g. spectra of minimal intensity where there was no material in the focal volume of the laser due to surface roughness, or spectral variation due to localized contaminants, were removed from the average by automatic outlier detection based on >10% of the spectrum being >2 standard deviations from the average, followed by recalculation of the average and standard deviation using remaining spectra. Background intensity was removed from each sample average by subtraction of a fitted polynomial function by linear least-squares regression, and the resulting spectrum was normalized to the maximum in the range 800–4000 cm^{-1} . See Fig. S1 in the Supplementary Information for a visualization of all processing steps. Raman peak positions and intensities were determined by sectioning the spectrum and fitting each peak with one or more Gaussian functions, with initial amplitude and position parameters given by their maxima and an initial width parameter of 20 cm^{-1} (see Figs. S2 and S3 in the SI).

3. Results and discussion

3.1. Distinguishing borates, carbonates, sulfates

The three main classes of evaporite mineral considered here exhibit very distinct Raman spectra under DUV excitation, as shown in Fig. 1. Colemanite (hydrated calcium borate), calcite (calcium carbonate) and gypsum (hydrated calcium sulfate) all exhibit unique patterns of peaks in the 900–1500 cm^{-1} region of their DUV Raman spectra. According to the literature on visible excitation Raman of borates, carbonates, and sulfates, the dominant Raman peaks are generally assigned to the internal vibrational modes of the oxyanion (Kloprogge and Frost, 1999; Bischoff et al., 1985; Mabrouk et al., 2013). The dominant peak in the region was at 1078 cm^{-1} for colemanite, 1079 cm^{-1} for calcite, and 1006 cm^{-1} for gypsum, and when combined with the detectable minor modes in the same region, these minerals can be very effectively

distinguished by their spectra. This is further reinforced by the clear detection of hydrated states in colemanite and gypsum, via the characteristically broad and intense O–H stretching modes of H_2O in the 3000–3600 cm^{-1} range.

For carbonate minerals such as calcite and the sulfate minerals like gypsum, the carbonate and sulfate ions possess very simple symmetries that result in only a single major peak around 950–1100 cm^{-1} and one or two minor peaks in the 800–1700 cm^{-1} region. These peaks are generally assigned to internal vibrational modes of the oxyanion, known as ν_1 (symmetric stretching), ν_2 (out-of-plane bending), ν_3 (anti-symmetric stretching), and ν_4 (in-plane bending) (Griffith, 1969). For calcite, the dominant peak at 1079 cm^{-1} is the ν_1 mode, a symmetric CO_3^{2-} stretching vibration; the second peak at 1430 cm^{-1} is ν_3 , the anti-symmetric CO_3^{2-} stretching vibration and the third peak at 1745 cm^{-1} is a combined stretching & bending vibration, $\nu_1 + \nu_4$ (Griffith, 1969; Gunasekaran et al., 2006). We note that the $\nu_1 + \nu_4$ assignment is somewhat contentious, with some papers in the literature assigning the ~ 1750 cm^{-1} peak instead to an overtone of the out-of-plane bending vibration, $2 \times \nu_2$ (Bischoff et al., 1985). For the sulfate mineral gypsum, the dominant peak at 1006 cm^{-1} is the ν_1 symmetric stretching vibration of SO_4^{2-} , the second peak at 1131 cm^{-1} is the ν_3 anti-symmetric vibration, while two broad overlapping peaks at ~ 3406 and ~ 3493 cm^{-1} are the symmetric and anti-symmetric O–H stretching vibrations of the hydrate (crystalline H_2O) unit (Griffith, 1969; Sarma et al., 1998). The borate mineral colemanite has a significant number of modes between 800 and 1700 cm^{-1} due to the complex symmetry of the polymerized borate ion $[\text{B}_3\text{O}_4(\text{OH})_3]^{2-}$, which contains interlocked polyhedral of trigonally and tetrahedrally coordinated boron (Jun et al., 1995; Kloprogge and Frost, 1999). The dominant peak of colemanite at 1078 cm^{-1} is assigned to the trigonal $[\text{BO}_3]$ symmetric stretching mode, a second peak at 1252 cm^{-1} is the B–O–H bending vibration, while a third peak at ~ 1602 cm^{-1} and a broad, strong peak at ~ 3204 cm^{-1} are the ν_2 (bending) and ν_1 (symmetric stretching) modes of H_2O , and finally a sharp, strong peak at ~ 3605 cm^{-1} that is assigned to the O–H stretching mode of hydroxyl groups on the polymerized borate ion (Kloprogge and Frost, 1999).

Though the DUV Raman spectrum of quartz has been reported by Czaja et al., this is the first description of DUV Raman spectra for many of these minerals and the peak positions observed tend to vary from those reported in the literature for these minerals under other excitation wavelengths (Czaja et al., 2009). Specifically, we find that the Raman peaks of colemanite, calcite, and gypsum are all at lower Raman shifts

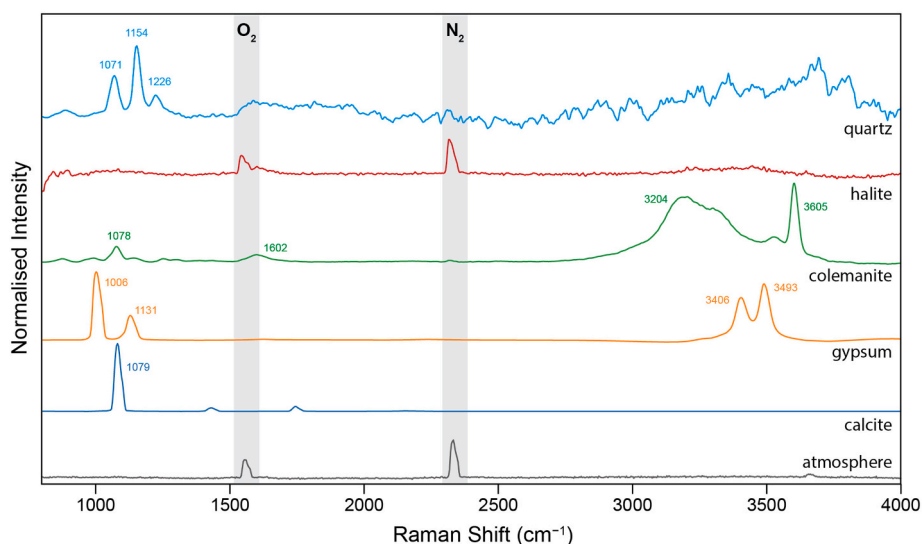


Fig. 1. Normalized DUV Raman spectra for the following minerals: colemanite (hydrated calcium borate), calcite (calcium carbonate) and gypsum (hydrated calcium sulfate), vs halite (NaCl) and quartz (SiO_2). Spectra have been offset for clarity.

under 248.6 nm excitation vs reported Raman shifts under longer-wavelength excitation. The trigonal [BO₃] stretching mode observed at 1078 cm⁻¹ in colemanite is down-shifted by ~6 cm⁻¹ vs a reported value of 1084 cm⁻¹ under 633 nm excitation (Frost et al., 2013). For calcite, the ν₁ mode at 1079 cm⁻¹ is down-shifted by 8–20 cm⁻¹ vs reported values of 1087 and 1099 cm⁻¹ under 515 nm and 633 nm excitation respectively (Griffith, 1969; Chan et al., 2017). The gypsum ν₁ mode at 1006 cm⁻¹ is down-shifted by ~0–2 cm⁻¹ vs 1008 cm⁻¹ (515 nm) and 1006 cm⁻¹ (633 nm) (Griffith, 1969; Sarma et al., 1998). Although Raman peak properties (particularly position) can vary with the chosen excitation wavelength for organic compounds (Sood et al., 2001; Quirico et al., 2009; Wood et al., 2017), this phenomenon is relatively unreported in minerals. As the deviation between our observed Raman shifts and literature values for visible excitation is a similar order of magnitude to our instrument's spectral resolution (~3.8 cm⁻¹) and we conclude that the deviation is a consequence of instrumental error and differences in calibration.

Such strong, distinctive spectra >800 cm⁻¹ are not universal amongst minerals, or representative of all evaporites. This is a consequence of both mineral structure and instrument architecture. For example, halite (NaCl) is a common evaporite mineral but it exhibits a Raman spectrum devoid of meaningful peaks, only background noise and atmospheric modes. The lack of peaks is a direct result of halite's lattice structure, which contains only monoatomic ions and no polarizable covalent bonds capable of undergoing Raman scattering. In addition to non-Raman active minerals, the MOBIUS and SHERLOC instruments are limited by the use of edge filters that cut off any signal from lattice modes below ~600 cm⁻¹. Silicate minerals such as quartz that are not evaporite minerals but do possess covalent bonds, exhibit their own unique DUV Raman spectra with a dominant peak reported to occur between 400 and 600 cm⁻¹ (Frosch et al., 2007). Unfortunately, this peak is obscured in our measurements by the edge filter and by overlap with a secondary NeCu laser emission line at ~700 cm⁻¹. However, we can still identify quartz (and potentially other silicates) by the pattern of Raman peaks in the 'mineral' peak region, such as the triplet of peaks observed for quartz at 1071, 1154, and 1226 cm⁻¹. We note that the signal-to-noise ratio (SNR) of these peaks was substantially lower than that of the evaporites investigated (e.g. 26:1 vs ~600:1 for calcite), due to their nature as relatively minor vibrational modes with small scattering cross-sections.

3.2. Variations between similar minerals

The sensitivity of Raman peaks to lattice structure and chemical composition means that the vibrational modes of a particular chemical unit, such as the carbonate ion, will appear slightly different in calcium carbonate vs magnesium carbonate or sodium carbonate. This provides the potential for distinguishing between similar minerals based on patterns of peak positions and relative intensities. Measured Raman shifts and relative intensities for the main peaks of each mineral are enumerated in Table 2.

Fig. 2 demonstrates the DUV Raman spectrum varies between a number of typical evaporite carbonate minerals. Where a mineral was available as both powdered and single-crystal samples, multiple spectra are shown as solid, dashed, or dotted lines overlaid to emphasize any variation between samples. We found that the exact position of the carbonate ion's dominant ν₁ mode varies significantly between ~1030 and ~1100 cm⁻¹ for the minerals considered, with trona appearing at the lowest frequency and dolomite at the highest. Only siderite did not produce a detectable ν₁ peak under the standard measurement conditions, a consequence of strong UV absorption by ionic Fe complexes (Chen et al., 1979), with a spectrum that shows only peaks attributed to atmospheric gases and reflected laser emission lines. For all other carbonates, variation in the frequency of internal modes for carbonates is not a phenomenon unique to DUV Raman, and has been described in both visible Raman and IR absorption spectra (Adler and Kerr, 1963; Kaabar et al., 2011; Chan et al., 2017). The origin of the variation lies in the electrostatic environment surrounding the oxyanion, such that the presence of a different metallic cation, or a change in crystallographic structure, will alter the electrostatic potentials experienced by the oxyanion, distorting the electron clouds of its constituent covalent bonds and altering the frequencies of their vibrations (D. Long, 1977). The vibrational spectra of carbonates are known to depend on the metallic cation's charge and ionic radius, but can be complicated by any concomitant changes in other properties; i.e. we do not always observe a simple linear or even monotonic relationship between metallic composition and ν₁ position. This is evidenced by the progression from 1079 cm⁻¹ for calcite (~100% Ca) to 1091 cm⁻¹ for dolomite (~50% Ca, ~50% Mg) to 1088 cm⁻¹ for magnesite (~100% Mg). This is because there is also a change in crystallographic structure between these three minerals, from hexagonal to rhombohedral to hexagonal respectively, which confounds the trend. Nevertheless, the position of the ν₁ peak can

Table 2

Raman peak positions (in cm⁻¹) for the major vibrational modes under DUV excitation for a number of borate, carbonate, and sulfate minerals, and their assignment to the internal vibrational modes of the oxyanion unit, or H₂O and OH⁻ units where applicable. Relative peak intensities are given in brackets, normalized to the dominant mode in the 800–1200 cm⁻¹ range. Key to assignments: ν_i = internal vibration *i*; *tet.* = tetrahedral borate; *trig.* = trigonal borate; *sym.* = symmetric; *asym.* = anti-symmetric; *S.* = stretching mode, *B.* = bending mode.

Borate assignments ^a	Colemanite	Kernite	Ulexite				
<i>tet. sym. S.</i>		930	972				
<i>trig. sym. S.</i>	1078						
B-O-H (<i>B.</i>)	1252 (0.19)	1320 (0.74)	1364 (0.55)				
H ₂ O ν ₂ (<i>B.</i>)	1602 (0.44)		1624 (0.27)				
H ₂ O ν ₁ (<i>S.</i>)	3204 (4.18)	3339 (4.42)	3416 (10.6)				
B-O-H (<i>S.</i>)	3605 (5.10)	3549 (10.1)	3569 (11.0)				
Carbonate assignments ^b	Calcite	Dolomite	Magnesite	Nahcolite	Rhodochrosite	Siderite	Trona
ν ₁ (<i>sym. S.</i>)	1079	1091	1088	1036	1078	N/A	1059
ν ₃ (<i>asym. S.</i>)	1430 (0.05)	1437 (0.08)	1440 (0.04)	1440 (0.20)	1410 (0.03)		1429 (0.15)
ν ₁ + ν ₄ (<i>S. + B.</i>)	1745 (0.07)	1753 (0.08)	1757 (0.09)	1680 (0.07)	1720 (0.10)		1718 (0.04)
Sulfate assignments ^c	Anhydrite	Barite	Epsomite	Gypsum	Melanterite	Natrojarosite	Thenardite
ν ₁ (<i>sym. S.</i>)	1010	979	1036	1006	1014	1006	983
ν ₃ (<i>asym. S.</i>)	1124 (0.33)	1135 (0.16)	1109 (0.26)	1131 (0.36)	1086 (0.67)	1146 (0.17)	1093 (0.17)
H ₂ O ν ₁ (<i>S.</i>)	3406 (0.11)		3359 (0.79)	3406 (0.73)	3426 (0.54)		
H ₂ O ν ₃ (<i>S.</i>)	3492 (0.15)			3493 (0.92)			
O-H (<i>S.</i>)							

^a Borate mineral peak assignments according to Klopogge and Frost (1999), Frost et al. (2013).

^b Carbonate mineral peak assignments from Griffith (1969), Chan et al. (2017).

^c Sulfate mineral peak assignments from Griffith (1969), Mabrouk et al. (2013).

be considered characteristic of that particular mineral and may be useful for direct identification, particularly when considered in coordination with the positions of the minor ν_3 and $\nu_1 + \nu_4$ modes at ~ 1430 and ~ 1750 cm^{-1} respectively (shown in Fig. 2, region B). While the ν_3 mode was relatively fixed in its position across different carbonate minerals, varying by 30 cm^{-1} between 1410 and 1440 cm^{-1} , the $\nu_1 + \nu_4$ peak position varied by 77 cm^{-1} from 1680 to 1757 cm^{-1} . This correlated well with position of the ν_1 mode (see Fig. S4 in the SI), which is consistent with its assignment as a combined $\nu_1 + \nu_4$ vibration and not as an overtone of the out-of-plane bending mode ν_2 . We also observe remarkable changes in the relative intensity of the two minor modes, both to the ν_1 peak and to each other. However, the $\nu_3/(\nu_1 + \nu_4)$ intensity ratio itself is not characteristic or diagnostic of the mineral in question, varying significantly between different samples of the same mineral – as demonstrated by both calcite and magnesite (Fig. 2, region B). The appearance of an additional peak in region B for trona and nahcolite (at 1560 and 1618 cm^{-1} respectively) can be attributed to their compositions, as both minerals contain some fraction of bicarbonate, a similar but structurally distinct oxyanion with its own slightly different internal vibrational modes. We also note that these two minerals exhibit the broadest, most down-shifted ν_1 peaks observed, at 1059 and 1036 cm^{-1} respectively, with nahcolite exhibiting a second strong peak at ~ 1263 cm^{-1} – tentatively assigned to the ν_1 mode of the bicarbonate ion, HCO_3^- .

Some carbonate spectra also exhibited peaks that could not be attributed to internal vibrational modes of the carbonate ion. Of the minerals examined, only powdered trona showed any vibrational evidence of hydration, exhibiting a strong, relatively narrow Raman peak at 3439 cm^{-1} that overlays a broad, relatively weak contribution around 3000 – 3400 cm^{-1} that can be attributed to more labile H_2O . Region B in Fig. 2 also reveals the appearance of a strong, broad peak for chalk calcite at ~ 1600 cm^{-1} , and a more minor peak at ~ 1390 cm^{-1} . The strong peak's position and shape are consistent with a resonant $\text{C}=\text{C}$ stretching mode, indicative of contamination by organic material – which is not unusual for a biogenic mineral such as chalk. Combined with the presence of the minor peak at ~ 1390 cm^{-1} , we conclude that the organic contaminant is a carbonaceous material such as kerogen, an insoluble mixture of macromolecular carbon rich in polyaromatic units that are typically formed by geothermal alteration of organic matter over geological timescales, and which is typically identified in Raman by a graphitic (G) mode at ~ 1600 cm^{-1} and a defect (D) mode at ~ 1350 cm^{-1} (Czaja et al., 2009; Quirico et al., 2009; Shkolyar et al., 2018). The relatively low intensity of this organic peak, comparable to the ν_3 mode,

suggests the contaminant must be low concentration, considering the very large Raman scattering cross-sections of aromatic organics under resonant DUV excitation (Asher, 1984; Wen and Thomas, 1998).

For the sulfate minerals, the ν_1 mode was observed to vary by ~ 57 cm^{-1} , between 979 and 1036 cm^{-1} (see Fig. 3). Like the carbonates, alterations in the frequency of the ν_1 mode is attributed to changes in the sulfate oxyanion's electrostatic environment, induced by substitution of the metallic cation, changes in crystallographic structure, and/or the degree of hydration. Although the sodium carbonates showed the lowest frequency ν_1 modes of the carbonate minerals investigated, we found that sodium sulfate (epsomite) exhibited the highest frequency ν_1 mode of the sulfate minerals. The minor peak at ~ 1120 cm^{-1} was assigned to the anti-symmetric ν_3 mode and showed a ~ 50 cm^{-1} variation in position between sulfates (between 1086 and 1135 cm^{-1}), but unlike the carbonates it was found to be relatively anti-correlated to the position of the ν_1 mode. Of the sulfate minerals studied, natrojarosite exhibited almost no detectable Raman signal, with the strongest signal observed coming from atmospheric N_2 at ~ 2330 cm^{-1} , and any mineral peaks in region A having significantly lower intensities that are close to the background noise level of the spectrum. As a consequence, there is significant uncertainty in the peak positions for the modes of natrojarosite recorded in Fig. 3 and Table 2.

Of the sulfate minerals considered here, only epsomite and melanterite exhibited the characteristically broad, strong peak of H_2O , with maxima at ~ 3359 and ~ 3426 cm^{-1} respectively, while gypsum and anhydrite exhibited a doublet of narrower H_2O peaks at ~ 3406 and ~ 3493 cm^{-1} . The broadness of the epsomite, melanterite H_2O band is typical of their high hydration state, i.e. having several H_2O units in different chemical environments exhibiting a broad range of vibrational frequencies, while the H_2O doublet for gypsum and anhydrite is typical of their low hydration state, i.e. fewer units with a more narrowly defined vibrational frequency. The appearance of H_2O in the anhydrite spectrum despite its formal definition as anhydrous calcium sulfate is a consequence of anhydrite's tendency to absorb ambient moisture over time, and the appearance of a weak H_2O doublet, identical in shape to that of gypsum ($\text{CaSO}_4 \cdot 2\text{H}_2\text{O}$), suggests that the hydrated fraction is in fact a minor gypsum component. When the sulfate and hydrate Raman peaks were integrated to obtain their total intensities, the hydrate/sulfate ratio was 0.52 for the anhydrite powder and 2.72 for the (pure) gypsum powder, which equates to the anhydrite containing a gypsum component of $\sim 19\%$ by mole. Subsequent XRD measurements established the anhydrite sample is $\sim 15\%$ gypsum.

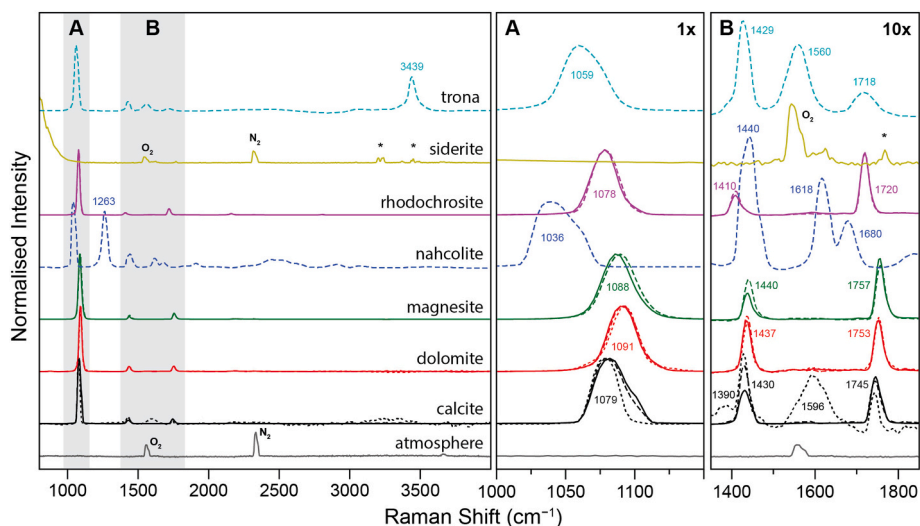


Fig. 2. Normalized DUV Raman spectra for various carbonate minerals, and the atmospheric standard spectrum. Mineral spectra are normalized to the maximum in the 800 – 1200 cm^{-1} region. Solid and dashed lines represent single-crystal and powdered mineral spectra respectively, dotted lines represent sedimentary calcite and dolomite rock. * indicates a known NeCu laser emission line.

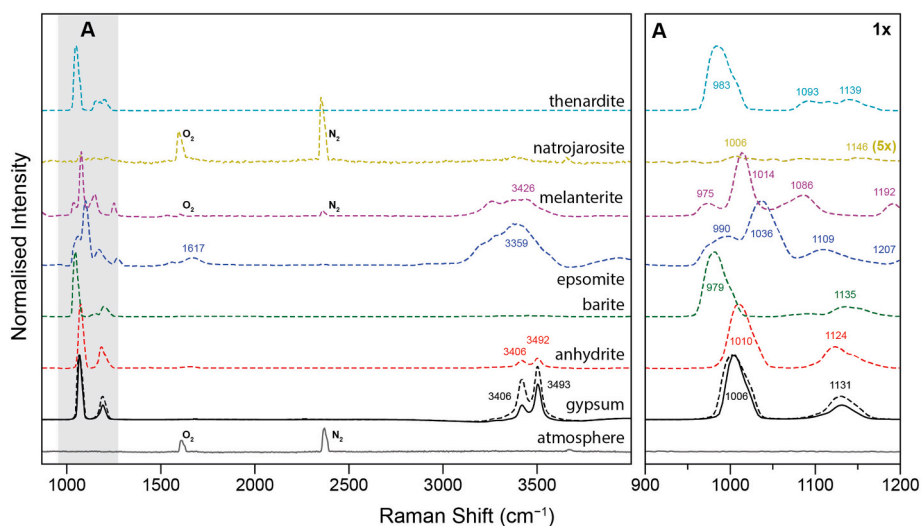


Fig. 3. Normalized DUV Raman spectra for various sulfate minerals, and the atmospheric standard spectrum. Each spectrum is normalized to the maximum in the 800–1200 cm^{-1} region. Solid and dashed lines represent single-crystal and powdered mineral spectra respectively.

The reduced Raman signal for carbonate/sulfate minerals containing iron (melanterite, natrojarosite, and siderite) has major implications for detection and identification of mineralogy and trace organics using DUV Raman spectroscopy, particularly on Mars. While the non-ferrous sulfate minerals had SNRs in excess of 2000:1, in melanterite the SNR was 1100:1 and in natrojarosite it was only 14:1. For the non-ferrous carbonates, the typical SNR was more than 400:1, but for siderite the mineral peaks were undetectable ($\text{SNR} < 5$). The reduced signal of ferrous minerals is unsurprising, a consequence of strong UV absorption by $\text{Fe}^{2+/3+}$ complexes around 200–300 nm (Chen et al., 1979). The presence of UV-absorbing Fe complexes will reduce the intensity of both the incident laser (at 248.6 nm) and any Raman-scattered light (at 255–275 nm) produced by other molecules/ions present within the sample. The extent of absorption will depend on the specific Fe complex present in the mineral and its absorption coefficients in the UV, reducing the effective penetration depth and the interrogation volume of the Raman measurement (Carrier et al., 2019; Razzell Hollis et al., 2020). In order to accurately and reliably account for the impact of UV absorption by iron, care must be taken to ascertain precisely what iron-containing minerals are present in a sample, and their UV absorption spectra. With such information, we may be able to correct for signal reduction

and determine the limits of detection for any other materials or organic compounds embedded within the mineral matrix (Razzell Hollis et al., 2020). The latter will be particularly important when searching for potential biosignatures on Mars, as organics may be present at a given concentration but undetectable depending on the nature and composition of the surrounding mineral matrix.

The borates colemanite, kernite and ulexite exhibited complex Raman spectra (Fig. 4) that are significantly different from one another in both the internal vibration region (800–1800 cm^{-1}) and the OH region (3000–3800 cm^{-1}). Unlike the carbonates and sulfates, these variations cannot be easily ascribed to their metallic composition, but are a consequence of dramatic differences in the internal structure of the polymerized borate unit between the three minerals. In colemanite, the borate unit is a triborate, $[\text{B}_3\text{O}_4(\text{OH})_3]^{2-}$, in kernite it is a pentaborate, $[\text{B}_5\text{O}_6(\text{OH})_6]^{3-}$, and in ulexite it is a tetraborate, $[\text{B}_4\text{O}_6(\text{OH})_2]^{2-}$. Each structure comprises a different combination of trigonally and tetrahedrally coordinated boron, and can vary in overall charge and degree of hydroxylation. Each structure will therefore possess a very different set of internal vibrational modes, resulting in a Raman spectrum that is highly characteristic. Detailed assignment of every peak is difficult, but generally we observe the symmetric stretching mode of tetrahedral

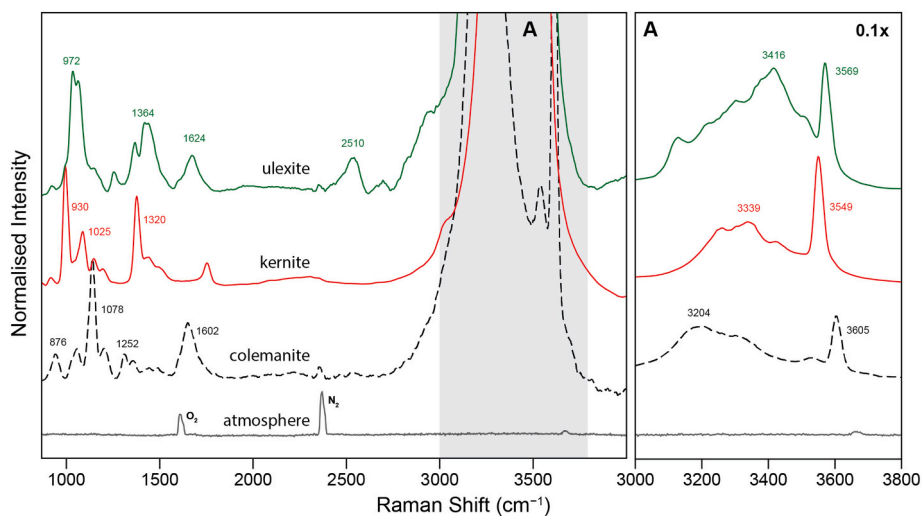


Fig. 4. Normalized DUV Raman spectra for three borate minerals and the atmospheric standard spectrum. Mineral spectra are normalized to the maximum in the 800–1600 cm^{-1} region. Solid and dashed lines represent single-crystal and powdered mineral spectra respectively.

[BO₃] around 950 cm⁻¹, the symmetric stretching mode of trigonal [BO₄] around 1080 cm⁻¹, the bending and stretching modes of B–OH around 1350 and 3580 cm⁻¹, with the exact positions and relative intensities being specific to that particular mineral (Klopprogge and Frost, 1999). All three borate minerals exhibited multiple peaks in each region, likely a result of different trigonal/tetrahedral units being vibrationally distinct depending on their location within each structure. Ulexite also exhibited a peak at 2510 cm⁻¹, which was unassigned.

The structure of the borate also had a marked impact on the pattern of H₂O stretching modes that comprise the broad peak around 3000–3600 cm⁻¹, with the exact position of the maximum varying from 3204 cm⁻¹ in colemanite to 3416 cm⁻¹ in ulexite. Perhaps the most diagnostic single peak is the B–OH stretching mode, which was consistently the strongest peak in the spectrum and exhibited a 56 cm⁻¹ variation in position (from 3549 to 3605 cm⁻¹) between the three minerals. The position of this peak was found to correlate well with the position of the dominant trigonal/tetrahedral mode around 900–1100 cm⁻¹, and as the OH bonds represent the exterior of the borate unit that are most likely to interact with surrounding metal ions and hydrate molecules, the position of the B–OH peak at ~3580 cm⁻¹ may be the most effective diagnostic peak for identifying the overall composition of a borate mineral.

3.3. Variations for a particular mineral

As is apparent in Fig. 2 and Fig. 3, there can be noticeable variations in the DUV Raman spectra between samples of the same mineral, depending on its bulk organization. Calcite, magnesite and gypsum all displayed marked differences in spectra between single-crystal and powdered polycrystalline samples, while the spectra of dolomite and rhodochrosite were unchanged. In each case the powdered sample was obtained from the same source as the single crystal and possesses the same bulk composition, which suggests that the vibrational changes are instead due to differences in long-range lattice order and anisotropy. Firstly, the reduction in SNR for a powdered sample vs the single crystal was on the order of 15–20%, with the exception of gypsum where it was ~80% (see Table 3). Most minerals exhibiting SNRs of similar order of magnitude suggests that the impact of greater light absorption/scattering by the particulate powder on the measured Raman intensity was fairly minor in most cases. We also found that there was a marked increase in the relative intensity of the carbonate/sulfate ν₃ peak for calcite, magnesite and gypsum when measured as powders vs single crystals. We believe this phenomenon is a consequence of the difference

Table 3

Spectral properties measured for different samples of calcite, dolomite, magnesite and rhodochrosite minerals. Signal-to-noise ratios were defined by the absolute intensity of the strongest peak in the spectrum, the internal vibration ν₁ of carbonate/sulfate, and the background noise at ~2000 cm⁻¹.

Mineral	Sample	SNR	ν ₁ frequency (cm ⁻¹)	ν ₃ intensity (relative to ν ₁)
Calcite	single crystal	595	1080	0.051
	powder	551	1078	0.088
	chalk	172	1078	0.098
Dolomite	single crystal	472	1091	0.078
	powder	371	1092	0.084
	rock	454	1092	0.073
Gypsum	single crystal	1976	1007	0.226
	powder	448	1006	0.359
Magnesite	single crystal	763	1087	0.040
	powder	602	1089	0.061
Rhodochrosite	single crystal	208	1078	0.030
	powder	201	1079	0.036

in anisotropy between powder and single crystals – the powdered polycrystalline sample is anisotropic and will therefore produce a consistent Raman signal independent of orientation, while the single crystal lattice will have a specific orientation during a measurement and the relative intensities of different vibrational modes will depend on the angles of their respective induced dipole moments with respect to the incident laser's polarization (Long, 1977; Basova, 1998). This has been previously reported and explained ab initio for single crystals of two phases of calcium carbonate: calcite and aragonite (de la Pierre et al., 2014).

In addition to a detectable difference in spectra between powder and single-crystals, we also observed that there was a variation in the ν₁ peak of calcite, between the three samples studied (single crystal, powder, and chalk). Namely, the ν₁ peak of chalk appeared narrow and symmetric, while the single crystal and powdered samples appeared broader and possessed a high-wavenumber shoulder around ~1100 cm⁻¹ (see Fig. 5). The full-width-half-maximum (FWHM) of the peak was found to be 20.7 cm⁻¹ for chalk, 28.6 cm⁻¹ for the single crystal and 26.3 cm⁻¹ for the powder. Deconvolving the peak using two Gaussian functions confirmed that the major component of all three peaks occurs at the same Raman shift (~1079 cm⁻¹) with similar FWHM of 20–23 cm⁻¹, and that the high-wavenumber shoulder is due to a second mode at ~1095 cm⁻¹, with a FWHM of ~20 cm⁻¹. Based on the integrated intensities of the deconvolved peaks in Fig. 5a, the shoulder represents about 30% of carbonate in both single crystal and powdered samples, and < 1% in chalk. No such shoulder was observed in dolomite, and the same deconvolution process resulted in a major component at ~1092 cm⁻¹ and negligible (<5%) minor component at ~1120 cm⁻¹. We hypothesize that the 1095 cm⁻¹ component in calcite indicates the presence of a minor elemental contaminant in the single crystal sample (and thus also in the powdered calcite) that was not present in the calcite chalk, and that this contaminant is responsible for perturbing the vibrations of surrounding carbonate ions. Although XRD could not detect the presence of trace crystallographic domains of any other mineral in the calcite, Mg-rich calcites are known to occur with Ca:Mg ratios approaching 1:1 and yet retain their calcite structure. The possibility of the shoulder originating in a low concentration of Mg is reinforced by the position of the contaminant peak, at 1095 cm⁻¹, which has its closest match in dolomite, ~1092 cm⁻¹, according to Table 2. The potential to detect minor elements in evaporite composition through deconvolution of Raman peaks could have very useful application to geology and planetary science, particularly when determining the origins and aqueous alteration of carbonates, e.g. the loss of Mg from calcite through diagenesis (Stanienda, 2016), without the need to remove, consume or otherwise damage the sample.

4. Conclusions

We have reported the first deep-ultraviolet Raman spectra for a number of minerals containing borate, carbonate, and sulfate that may be found in evaporite deposits, and are highly relevant to lacustrine and fluvial environments on Earth and Mars. We have demonstrated that these minerals exhibit DUV Raman spectra that are dominated by the vibrational modes of the polyatomic oxyanion, and are readily distinguishable even between minerals that differ only in their metallic cation, such as calcite and dolomite, due to modulation of vibrational frequencies and relative intensities. Furthermore, the evaporites provide extremely strong Raman spectra compared to other minerals such as halite and quartz, a consequence of strong scattering by the polyatomic oxyanion and the relative UV transparency of these minerals. However, the presence of Fe^{2+/3+} complexes in certain minerals, such as siderite and natrojarosite, will act to absorb UV light and reduce the measured signal significantly. This confirms that the presence of Fe complexes in a mineral matrix will have profound implications for our ability to detect trace organics that may be preserved in the mineral during deposition/evaporation.

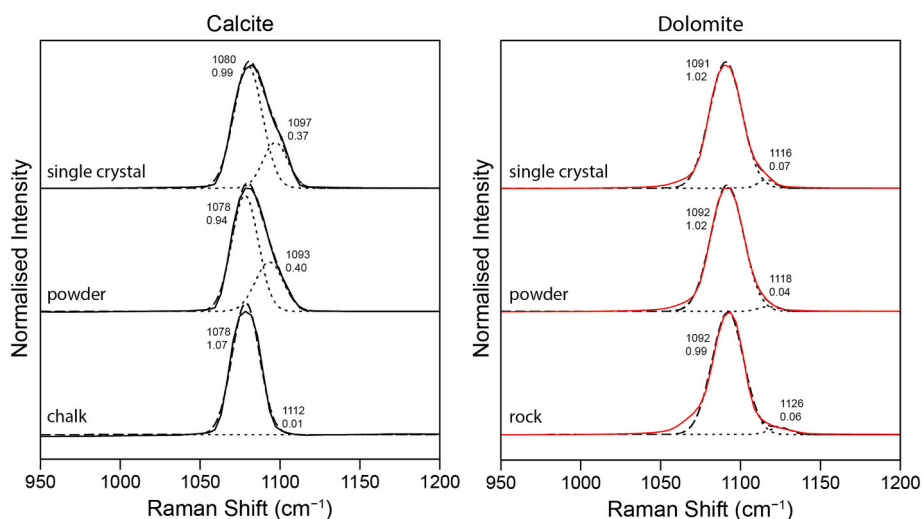


Fig. 5. Normalized DUV Raman spectra around the internal vibration ν_1 peak for a) calcite, and b) dolomite, in three different physical formations: as a single-crystal, a powder and as sedimentary chalk/rock. For each peak, a best fit (dashed line) using two gaussian functions (dotted lines) were plotted with the individual functions' positions and amplitudes.

We believe that this work represents an important step towards the construction of a spectral library for DUV Raman that is relevant to planetary science, particularly astrobiology, that has so far focused on obtaining standard spectra of organic compounds and silicate minerals. The ability to distinguish different kinds of evaporite based on the mineral standards described in this paper will be essential to interpreting DUV Raman spectra of mineralogical samples, particularly when searching for trace organic contributions that may be obscured by overlap with the spectrum of the mineral matrix. Indeed, subtraction of the mineral spectrum will only be possible if the mineral can be identified, and its spectrum is well known.

Supplementary data to this article can be found online at <https://doi.org/10.1016/j.icarus.2020.114067>.

Acknowledgements

The work described in this paper was carried out at the Jet Propulsion Laboratory, California Institute of Technology, under a contract with the National Aeronautics and Space Administration. This work was funded by a NASA Postdoctoral Program fellowship awarded to Joseph Razzell Hollis, administered by the Universities Space Research Association on behalf of NASA. The authors would also like to thank Dr. Robert Anderson (NASA JPL) for the use of his Bruker X-ray Diffractometer. © 2019. California Institute of Technology. Government sponsorship acknowledged.

References

- Abbey, W.J., Bhartia, R., Beegle, L.W., Deflores, L., Paez, V., Sijapati, K., et al., 2017. Deep UV Raman spectroscopy for planetary exploration: The search for in situ organics. *Icarus* 290, 201–214. <https://doi.org/10.1016/j.icarus.2017.01.039>.
- Adler, H.H., Kerr, P.F., 1963. Infrared absorption frequency trends for anhydrous normal carbonates. *Am. Mineral.* 48, 124–137.
- Asher, S.A., 1984. Ultraviolet resonance Raman spectrometry for detection and speciation of trace polycyclic aromatic hydrocarbons. *Anal. Chem.* 56, 720–724. <https://doi.org/10.1021/ac00268a029>.
- Asher, S.A., 1993. UV resonance Raman spectroscopy for analytical, physical, and biophysical chemistry. *Anal. Chem.* 65, 210A–210A. <https://doi.org/10.1021/ac00052a715>.
- Basova, T., 1998. Raman polarization studies of the orientation of molecular thin films. *Thin Solid Films* 325, 140–144. [https://doi.org/10.1016/S0040-6090\(98\)00485-4](https://doi.org/10.1016/S0040-6090(98)00485-4).
- Beegle, L., Bhartia, R., White, M., Deflores, L., Abbey, W., Wu, Y.H., et al., 2015. SHERLOC: Scanning habitable environments with Raman & luminescence for organics & chemicals. In: IEEE Aerospace Conference Proceedings. <https://doi.org/10.1109/AERO.2015.7119105>.
- Bischoff, W.D., Sharma, S.K., Mackenzie, F.T., 1985. Carbonate ion disorder in synthetic and biogenic magnesium calcites: A Raman spectral study. *Am. Mineral.* 70, 581–589.
- Boynton, W.V., Ming, D.W., Kounaves, S.P., Young, S.M.M., Arvidson, R.E., Hecht, M.H., Hoffman, J., Niles, P.B., Hamara, D.K., Quinn, R.C., Smith, P.H., Sutter, B., Catling, D.C., Morris, R.V., 2009. Evidence for calcium carbonate at the Mars Phoenix landing site. *Science* 325 (5936), 61–64.
- Carrier, B.L., Abbey, W.J., Beegle, L.W., Bhartia, R., Liu, Y., 2019. Attenuation of ultraviolet radiation in rocks and minerals: Implications for Mars science. *J. Geophys. Res. Planets* 124, 2599–2612. <https://doi.org/10.1029/2018JE005758>.
- Chan, Q.H.S., Zolensky, M.E., Bodnar, R.J., Farley, C., Cheung, J.C.H., 2017. Investigation of organo-carbonate associations in carbonaceous chondrites by Raman spectroscopy. *Geochim. Cosmochim. Acta* 201, 392–409. <https://doi.org/10.1016/j.gca.2016.10.048>.
- Chen, Y., Shaked, D., Banin, A., 1979. The role of structural iron(III) in the UV absorption by Smectites. *Clay Miner.* 14, 93–102.
- Czaja, A.D., Kudryavtsev, A.B., Cody, G.D., Schopf, J.W., 2009. Characterization of permineralized kerogen from an Eocene fossil fern. *Org. Geochem.* 40, 353–364. <https://doi.org/10.1016/j.orggeochem.2008.12.002>.
- De La Pierre, M., Carteret, C., Maschio, L., André, E., Orlando, R., Dovesi, R., 2014. The Raman spectrum of CaCO₃ polymorphs calcite and aragonite: A combined experimental and computational study. *J. Chem. Phys.* 140, 164509. <https://doi.org/10.1063/1.4871900>.
- Ehlmann, B.L., Edwards, C.S., 2014. Mineralogy of the Martian surface. *Annu. Rev. Earth Planet. Sci.* 42 (1) <https://doi.org/10.1146/annurev-earth-060313-055024>.
- Ehlmann, B.L., Mustard, J.F., Murchie, S.L., Poulet, F., Bishop, J.L., Brown, A.J., Calvin, W.M., Clark, R.N., Des Marais, D.J., Milliken, R.E., Roach, L.H., Roush, T.L., Swayze, G.A., Wray, J.J., 2008. Orbital identification of carbonate-bearing rocks on Mars. *Science* 322 (5909), 1828–1832.
- Frosch, T., Tarcea, N., Schmitt, M., Thiele, H., Langenhorst, F., Popp, J., 2007. UV Raman imaging - A promising tool for astrobiology: Comparative Raman studies with different excitation wavelengths on SNC Martian meteorites. *Anal. Chem.* 79, 1101–1108.
- Frost, R.L., Xi, Y., Scholz, R., Maria Belotti, F., Cândido Filho, M., 2013. Infrared and Raman spectroscopic characterization of the borate mineral colemanite – CaB₃O₄(OH)₃·H₂O – implications for the molecular structure. *J. Mol. Struct.* 1037, 23–28. <https://doi.org/10.1016/j.molstruc.2012.11.047>.
- Gasda, P.J., Haldeman, E.B., Wiens, R.C., Rapin, W., Bristow, T.F., et al., 2017. In situ detection of boron by ChemCam on Mars. *Geophys. Res. Lett.* 44, 8739–8748. <https://doi.org/10.1002/2017GL074480>.
- Griffith, W.P., 1969. Raman spectroscopy of minerals. *Nature* 224, 264–266.
- Gunasekaran, S., Anbalagan, G., Pandi, S., 2006. Raman and infrared spectra of carbonates of calcite structure. *J. Raman Spectrosc.* 37, 892–899. <https://doi.org/10.1002/jrs.1518>.
- Hays, L. E., Graham, H. V., Des Marais, D. J., Hausrath, E. M., Horgan, B., McCollom, T. M., et al. (2017). Biosignature preservation and detection in Mars analog environments. *Astrobiology* 17, 363–400. <https://doi.org/10.1089/ast.2016.1627>.
- Jones, E., Oliphant, E., Peterson, P., et al., 2001. SciPy: Open Source Scientific Tools for Python. Available at: <http://www.scipy.org/>. (Accessed 20 July 2018).
- Jun, L., Shuping, X., Shiyang, G., 1995. FT-IR and Raman spectroscopic study of hydrated borates. *Spectrochim. Acta* 51A, 519–532.
- Kaabar, W., Bott, S., Devonshire, R., 2011. Raman spectroscopic study of mixed carbonate materials. *Spectrochim. Acta Part A Mol. Biomol. Spectrosc.* 78, 136–141. <https://doi.org/10.1016/j.saa.2010.09.011>.
- Kim, H.-J., Furukawa, Y., Kakegawa, T., Bita, A., Scorei, R., Benner, S.A. (2016). Evaporite borate-containing mineral ensembles make phosphate available and

- regiospecifically phosphorylate ribonucleosides: Borate as a multifaceted problem solver in prebiotic chemistry. *Angew. Chem. Int. Ed.* 55, 15816–15820. <https://doi.org/10.1002/anie.201608001>.
- Kloprogge, J.T., Frost, R.L., 1999. Raman microscopic study of some borate minerals: Ulexite, kernite, and inderite. *Appl. Spectrosc.* 53, 356–364.
- Long, D.A., 1977. *Raman Spectroscopy*. McGraw Hill, London.
- Mabrouk, K.B., Kauffmann, T.H., Aroui, H., Fontana, M.D., 2013. Raman study of cation effect on sulfate vibration modes in solid state and in aqueous solutions. *J. Raman Spectrosc.* 44, 1603–1608.
- Newville, M., Stensitzki, T., Allen, D.B., Ingargiola, A., 2014. LMFIT: Non-Linear Least-Square Minimization and Curve-Fitting for Python. Available at: <https://lmfit.github.io/lmfit-py/index.html>. (Accessed 10 March 2018).
- Niles, P.B., Catling, D.C., Berger, G., Chassefiere, E., Ehlmann, B.L., Michalski, J.R., Morris, R., Ruff, S.W., Sutter, B., 2013. Geochemistry of carbonates on Mars: Implications for climate history and nature of aqueous environments. *Space Sci. Rev.* 174 (1–4), 301–328.
- Osterloo, M.M., Anderson, F.S., Hamilton, V.E., Hynek, B.M., 2010. Geologic context of proposed chloride-bearing materials on Mars. *J. Geophys. Res.* 115, E10012 <https://doi.org/10.1029/2010JE003613>.
- Quirico, E., Montagnac, G., Rouzaud, J.N., Bonal, L., Bourot-Denise, M., Duber, S., et al., 2009. Precursor and metamorphic condition effects on Raman spectra of poorly ordered carbonaceous matter in chondrites and coals. *Earth Planet. Sci. Lett.* 287, 185–193. <https://doi.org/10.1016/j.epsl.2009.07.041>.
- Razzell Hollis, J., Rheingold, D.A., Bhartia, R., Beegle, L.W., 2020. An optical model for quantitative Raman microspectroscopy. *Appl. Spectrosc.* <https://doi.org/10.1177/0003702819895299>.
- Sapers, H.M., Razzell-Hollis, J., Bhartia, R., Beegle, L.W., Orphan, V.J., Amend, J.P., et al., 2019. The cell and the sum of its parts: Patterns of complexity in biosignatures as revealed by deep UV Raman spectroscopy. *Front. Microbiol.* 10, 1–15. <https://doi.org/10.3389/fmicb.2019.00679>.
- Sarma, L.P., Prasad, P.S.R., Ravikumar, N., 1998. Raman spectroscopic study of phase transitions in natural gypsum. *J. Raman Spectrosc.* 29, 851–856.
- Shkolyar, S., Eshelman, E.J., Farmer, J.D., Hamilton, D., Daly, M.G., Youngbull, C., 2018. Detecting kerogen as a biosignature using collocated UV time-gated Raman and fluorescence spectroscopy. *Astrobiology* 18, 431–454. <https://doi.org/10.1089/ast.2017.1716>.
- Sood, A.K., Gupta, R., Asher, S.A., 2001. Origin of the unusual dependence of Raman D band on excitation wavelength in graphite-like materials. *J. Appl. Phys.* 90, 4494–4497. <https://doi.org/10.1063/1.1408590>.
- Stanienda, K.J., 2016. Carbonate phases rich in magnesium in the Triassic limestones of the eastern part of the Germanic Basin. *Carbonates Evaporites* 31, 387–405. <https://doi.org/10.1007/s13146-016-0297-2>.
- Stephenson, J.D., Hallis, L.J., Nagashima, K., Freeland, S.J., 2013. Boron enrichment in Martian clay. *PLoS One* 8 (6), e64624. <https://doi.org/10.1371/journal.pone.0064624>.
- Uckert, K., Bhartia, R., Michel, J., 2019. A semi-autonomous method to detect cosmic rays in Raman hyperspectral data sets. *Appl. Spectrosc.* <https://doi.org/10.1177/0003702819850584>.
- van der Walt, S., Colbert, S.C., Varoquaux, G., 2011. The NumPy array: A structure for efficient numerical computation. *Comput. Sci. Eng.* 13, 22–30. <https://doi.org/10.1109/MCSE.2011.37>.
- Vaniman, D.T., Bish, D.L., Ming, D.W., Bristol, T.F., Morris, R.V., et al., 2013. Mineralogy of a mudstone at Yellowknife Bay, Gale Crater. *Mar. Sci.* 342 <https://doi.org/10.1126/science.1243480>.
- Wen, Z.Q., Thomas, G.J., 1998. UV resonance Raman spectroscopy of DNA and protein constituents of viruses: Assignments and cross sections for excitations at 257, 244, 238, and 229 nm. *Biopolymers* 45, 247–256.
- Westall, F., Bost, N., Vago, J.L., Kminek, G., Campbell, K.A., 2015. Biosignatures on Mars: What, where, and how? Implications for the search for Martian life. *Astrobiology* 15, 998–1029. <https://doi.org/10.1089/ast.2015.1374>.
- Wood, S., Razzell Hollis, J., Kim, J.-S., 2017. Raman spectroscopy as an advanced structural nanoprobe for conjugated molecular semiconductors. *J. Phys. D: Appl. Phys.* 50, 73001. <https://doi.org/10.1088/1361-6463/50/7/073001>.